
OPTIMIZATION-EMBEDDED ACTIVE MULTI-FIDELITY SURROGATE LEARNING FOR MULTI-CONDITION AIRFOIL SHAPE OPTIMIZATION

Isaac Robledo

Aerial Platforms Department
Subdirecció General for Aeronautical Systems
Spanish National Institute for Aerospace Technology (INTA)

Department of Aerospace Engineering
Universidad Carlos III de Madrid
Madrid, Spain
isaac.robledo@alumnos.uc3m.es

Alberto Vilarino

Department of Aerospace Engineering
Universidad Carlos III de Madrid
Madrid, Spain
alberto.vilarino@alumnos.uc3m.es

Arnau Miró

TUAREG Research Group
Universitat Politècnica de Catalunya (UPC)
CASE Large-Scale Computational Fluid Dynamics
Barcelona Supercomputing Centre (BSC)
Barcelona, Spain
arnau.miro@upc.edu

Oriol Lehmkuhl

CASE Large-Scale Computational Fluid Dynamics
Barcelona Supercomputing Centre (BSC)
Barcelona, Spain
oriol.lehmkuhl@bsc.es

Carlos Sanmiguel Vila

Aerial Platforms Department
Subdirecció General for Aeronautical Systems
Spanish National Institute for Aerospace Technology (INTA)

Department of Aerospace Engineering
Universidad Carlos III de Madrid
Madrid, Spain
csanvil@inta.es

Rodrigo Castellanos

Department of Aerospace Engineering
Universidad Carlos III de Madrid
Madrid, Spain
rcastell@ing.uc3m.es

ABSTRACT

Active multi-fidelity surrogate modeling is developed for multi-condition airfoil shape optimization to reduce high-fidelity CFD cost while retaining RANS-level accuracy. The framework couples a low-fidelity-informed Gaussian process regression transfer model with uncertainty-triggered sampling and a synchronized elitism rule embedded in a hybrid genetic algorithm. Low-fidelity XFOIL evaluations provide inexpensive features, while sparse RANS simulations are adaptively allocated when predictive uncertainty exceeds a threshold; elite candidates are mandatorily validated at high fidelity, and the population is re-evaluated to prevent evolutionary selection based on outdated fitness values produced by earlier surrogate states. The method is demonstrated for a two-point problem at $Re = 6 \times 10^6$ with cruise at $\alpha = 2^\circ$ (maximize $E = L/D$) and take-off at $\alpha = 10^\circ$ (maximize C_L) using a 12-parameter CST representation. Independent multi-fidelity surrogates per flight condition enable decoupled refinement. The optimized design improves cruise efficiency by 41.05% and take-off lift by 20.75% relative to the best first-generation individual. Over the full campaign, only 14.78% (cruise) and 9.5% (take-off) of evaluated individuals require RANS, indicating a substantial reduction in high-fidelity usage while maintaining consistent multi-point performance.

1 Introduction

Advances in computational aerodynamics have made automated shape optimization a viable component of modern design workflows. Compared with traditional cycles dominated by wind-tunnel testing and empirical iteration, CFD-driven optimization enables systematic exploration with fewer simplifying assumptions. Its practical deployment, however, is constrained by the high dimensionality typical of aerodynamic design spaces and by the cost of repeated high-fidelity evaluations. These constraints motivate surrogate-based global optimization frameworks that manage fidelity adaptively, combining low-cost models with targeted high-fidelity corrections.

Historically, shape optimization has relied on gradient-based methods coupled with adjoint equations [1, 2]. Although computationally efficient in terms of design-variable scaling, these approaches typically require a tight integration between the flow solver and the optimizer, which often leads to problem-specific implementations and limits portability in industrial settings [3]. To overcome these limitations, the field has increasingly adopted surrogate modeling. Trained on an initial set of simulations, surrogate models provide inexpensive predictions across the design space, which facilitates the use of global, derivative-free optimizers [4]. Among the various surrogate options, Kriging remains one of the most widely used surrogate choices in aerodynamic design [5, 6]. However, its standard formulations can become computationally expensive to train and deploy for high-dimensional inputs or large datasets [7]. To mitigate these costs, Kriging is typically coupled with gradient information [8, 9] or employ partial least squares to reduce training costs [10].

Building on these traditional frameworks, recent advancements in surrogate-based optimization have integrated machine learning models as high-capacity physics evaluators. This shift aims to further reduce reliance on repeated CFD simulations, offering substantial gains in evaluation speed, albeit often at the expense of fidelity relative to high-fidelity solvers. Representative examples include fully connected neural networks [11] or convolutional neural networks [12] for aerodynamic coefficient prediction, Physics-Informed Neural Networks (PINNs) for physics-constrained inference [13], and DeepONets [14], which enable mesh-independent operator learning [15]. More advanced methodologies lean towards merging these techniques; for example, Pereira et al. [16] couples Generative Adversarial Network (GAN) based parameterization with CNN coefficient prediction for supersonic airfoil shape optimization, while Liu et al. [17] uses a deep reinforcement learning (DRL) procedure to integrate CNN-based parametric extraction with PINN aerodynamic evaluation.

Parallel to these advancements in predictive modeling, the problem of geometric parametrization remains a critical bottleneck, as the choice of representation directly dictates the design-space dimensionality and the feasibility of generated shapes. In airfoil optimization, classical meth-

ods have long relied on B-spline and Bézier representations [18], PARSEC [19], Hicks-Henne bump functions [20], and shape-class transformation (CST) [21, 22, 23]. More recently, data-driven methods have introduced dimensionality reduction and generative modeling into airfoil parametrization. Approaches range from projection-based solutions using Proper Orthogonal Decomposition (POD) [24, 25, 26] to nonlinear latent-variable model techniques such as Variational Autoencoders (VAE) [27] and GAN [28]. Other strategies focus on learning parametrizations directly, for example through GAN-based shape generation [29], or on extracting compact parametric descriptions from existing data [30].

Both surrogate modeling and shape parametrization aim to mitigate the inherent complexity, non-convexity, and high dimensionality of aerodynamic shape optimization, either by reducing the effective design space through parametrization or by accelerating evaluations through surrogate modeling. Multi-fidelity techniques address this challenge from a complementary perspective by combining information sources of differing cost and reliability. In this paradigm, a large number of inexpensive low-fidelity evaluations are exploited to explore the design space, while a limited set of high-fidelity simulations is employed to correct their deficiencies, enabling improved performance estimates at reduced computational cost [31, 32].

To implement this multi-fidelity paradigm, research has traditionally branched into two distinct architectural strategies. The first involves hierarchical approaches, which selectively invoke different fidelity levels depending on the design stage or region of interest; however, these can incur in increasing algorithmic complexity and reduced interpretability as the number of information sources grows [31]. In contrast, surrogate-based multi-fidelity models seek to fuse available information into a unified predictive framework. Because this approach offers a balance of accuracy and efficiency, it serves as the basis for the methodology developed in this study. Early formulations relied on additive or multiplicative corrections to low-fidelity predictions, $\hat{y}_{HF}(x) = \rho(x) y_{LF}(x) + \delta(x)$, where ρ and δ are fitted correction terms. Representative examples in aeronautics include the additive model of Alexandrov et al. [33] and the multiplicative formulation of Balabanov et al. [34], later extended through more flexible weighting and regression strategies [35, 36].

With the adoption of modern machine-learning techniques, multi-fidelity surrogate modeling has received increasing attention in aerodynamics, where the non-linearity of the governing equations and the diversity of available fidelity sources (from panel methods to RANS, LES, DNS, and experimental data) challenge classical correction strategies [37, 32]. Among these approaches, co-Kriging is a widely used framework, as it can exploit statistical correlations between fidelity levels to construct improved predictors [38, 39, 40, 41]. Deep learning has also been used to construct multi-fidelity models, including multi-fidelity neural networks [42], multi-fidelity deep Bayesian neural

networks [43], multi-fidelity deep Gaussian processes [44], multi-fidelity deep neural operators [45], and multi-fidelity reinforcement learning [46]. For the interested reader, a broader survey on multi-fidelity surrogate models for optimization is provided by Li and Li [47].

However, despite their success, many existing multi-fidelity surrogates are constructed offline and subsequently assumed to remain valid throughout the optimization process. This assumption becomes fragile in large, weakly constrained design spaces, where optimizers push the search toward unexplored regions and potentially distinct physical regimes. Under these conditions, the correlation between low- and high-fidelity models may locally deteriorate, and static correction models can rapidly lose reliability. These limitations motivate multi-fidelity strategies that not only fuse heterogeneous information sources but also adapt dynamically as the optimization progresses.

Active learning strategies address the limitations of static surrogate models by iteratively adapting them through the targeted acquisition of new training data. In this context, Bayesian optimization is a prominent example, where uncertainty-aware acquisition functions guide sample selection to improve model accuracy while supporting optimization. Motivated by this paradigm, extensive research has focused on integrating active learning into multi-fidelity aerodynamic optimization frameworks. Representative examples include partitioning candidate designs between low- and high-fidelity evaluators within an optimization loop [48], uniform infilling strategies embedded in multi-fidelity shape optimization [49], and expected-improvement-driven enrichment in co-Kriging-based airfoil optimization [50]. More generally, adaptive infill strategies have shown strong performance by selecting additional samples aimed at improving surrogate reliability in the region of interest [51, 52, 53, 54].

Despite these advances, most existing approaches treat active learning primarily as a surrogate-improvement mechanism rather than as a process coupled to the optimizer’s evolving search dynamics. In practice, high-fidelity evaluations are typically allocated through predefined schedules, fixed per-iteration budgets, or acquisition rules applied globally. As a result, these strategies may not adapt fidelity selection to the local reliability of the surrogate along the optimizer trajectory, and they only indirectly account for the evolving structure of the optimization landscape. In large, multi-modal design spaces, where the search progressively concentrates around high-performing regions and may encounter distinct physical regimes, such enrichment policies can lead to inefficient allocation of computational resources and delayed correction of surrogate inaccuracies. These limitations motivate active multi-fidelity strategies in which uncertainty quantification directly governs fidelity selection and model refinement throughout the optimization process.

In this work, we propose an optimization-embedded active multi-fidelity framework for multi-condition airfoil shape optimization that couples surrogate modeling, un-

certainty quantification, and evolutionary search within a unified process. The core mechanism is an uncertainty-triggered high-fidelity evaluation strategy: rather than prescribing high-fidelity calls a priori, expensive simulations are allocated dynamically based on the local reliability of the evolving multi-fidelity surrogate. High-fidelity evaluations are therefore invoked only when needed, enabling iterative correction of the surrogate as the optimizer explores new regions of the design space. Furthermore, the framework introduces a condition-wise decoupling of the multi-fidelity models, allowing the optimization to simultaneously account for multiple flight conditions, each with its own uncertainty structure and refinement requirements. This feature is particularly relevant in multi-point aerodynamic design, where the correlation between low- and high-fidelity models may differ substantially across operating regimes.

Multi-fidelity fusion is here formulated as a data-driven transfer mapping rather than a hierarchical autoregressive model. Specifically, the high-fidelity response is learned as a nonparametric function of the design variables and the associated low-fidelity outputs, which avoids assuming a globally valid linear correlation between fidelity levels. Active learning is then used to introduce high-fidelity corrections in regions where the low-to-high relationship degrades along the optimization trajectory.

The proposed active multi-fidelity strategy is embedded within a hybrid global evolutionary optimizer, HyGO [55], which provides synchronization between the evolving population and the adaptive fidelity-selection process. This integration supports robust global search over large, weakly constrained design spaces, while ensuring consistency between the surrogate models, the objective evaluations, and the evolutionary dynamics. The implementation in HyGO removes the need for fixed per-iteration high-fidelity budgets by making fidelity escalation a candidate-level decision driven by surrogate uncertainty, and it includes an elite-consistency mechanism to avoid selection drift after surrogate updates.

The proposed approach is demonstrated on a two-condition airfoil shape optimization problem using a 12-parameter CST representation, combining XFOIL and RANS simulations. The results provide quantitative evidence of surrogate convergence during optimization, reductions in high-fidelity cost through adaptive refinement, and physically interpretable aerodynamic trends, illustrating the behavior of the proposed strategy on a multi-condition airfoil design problem.

The main contributions of this work are threefold: (i) an optimization-embedded active multi-fidelity strategy in which high-fidelity calls are triggered by uncertainty rather than by a fixed schedule; (ii) a condition-wise decoupled surrogate architecture enabling independent refinement across operating points; and (iii) a two-condition CST-based airfoil optimization study combining panel method (LF) and RANS (HF), including cost and convergence analyses.

Table 1: Parametric domain for the 12 parameter CST representation.

Parameter	Upper Limit	Lower Limit
θ_1	0.60377	0.03834
θ_2	0.70389	-0.35002
θ_3	0.79453	-0.53920
θ_4	0.81549	-0.42392
θ_5	0.89804	-1
θ_6	1	-1
θ_7	0.29979	-0.38389
θ_8	0.53284	-0.55331
θ_9	0.36506	-0.77029
θ_{10}	0.60049	-0.62099
θ_{11}	0.38495	-0.79700
θ_{12}	0.86272	-1

The remainder of this paper is organized as follows. [Section 2](#) presents the proposed methodology, including the airfoil parametrization, the numerical setup of the low- and high-fidelity solvers, the multi-fidelity surrogate modeling strategy, and the optimization-embedded active learning framework. [Section 3](#) discusses the results of the multi-condition airfoil optimization campaign, including convergence behavior, computational cost analysis, surrogate validation, and physical interpretation of the optimized geometries. Finally, [section 4](#) summarizes the main conclusions and outlines perspectives for future developments.

2 Methodology

This section details the methodology proposed for the multi-fidelity airfoil optimization framework. The discussion is organized into four main components: the geometric parametrization used to define the airfoil shape, the numerical setup of the low- and high-fidelity CFD solvers, the definition of the multi-fidelity surrogate environment, and the genetic algorithm-based optimization strategy.

2.1 Airfoil Parametrization

Airfoil shape parametrization is a pivotal aspect of any shape optimization framework, as it defines the parametrization and dimensionality of the design space. This study employs the CST methodology [21] for its flexibility, robustness, and ability to represent a broad range of shapes with a concise set of parameters. The airfoil geometry is defined by a class function (defining the general airfoil shape) and a shape function (typically Bernstein polynomials). The coefficients of these polynomials serve as the design variables. For this study, a 12-parameter representation was selected (six coefficients for the upper surface, six for the lower), offering a trade-off between geometric flexibility and low dimensionality for the optimization algorithm.

Defining the parametric domain (i.e., the bounds of the design variables) is critical. To ensure the domain en-

Table 2: Geometrical constraints for CST-generated airfoils with unitary chord

Target	Constraint	Valid Range
Global geometric bounds	Maximum thickness	5%-50%
	Maximum thickness x -position	20%-35%
	Contiguous panels angle in upper surface	$< 10^\circ$
TE geometry	Minimum thickness in TE vicinity	0.2%
	Minimum x for collapsed thickness	96%
	Minimum thickness region	88%-96%
	Minimum TE angle	3°
	Monotonicity in TE region	True
Undesired shapes	Minimum airfoil area	$0.02 \cdot t_{max}$

compasses realistic aerodynamic shapes, a broad reference database spanning multiple airfoil families was assembled, including the NACA 4- and 5-digit series, and representative profiles from NACA 6-series, RAE, DAE, RAG, Boeing, Whitcomb, NLF, ONERA, and the Eppler E398 and SC families. All airfoils were then fitted using the CST formulation. This procedure reproduces established aerodynamic shapes while allowing for intermediate geometries beyond the original family definitions. To balance exploration and feasibility, the CST bounds inferred from this dataset were expanded by 15% on both sides. The resulting parametric domain is detailed in [Table 1](#), where θ_1 - θ_6 correspond to the upper surface and θ_7 - θ_{12} to the lower surface, and $\Theta = [\theta_1, \dots, \theta_{12}]$ is the parametric vector characterizing a specific airfoil shape. Despite this bounded domain, specific coefficient combinations may still yield degenerate geometries (e.g., self-intersecting surfaces or zero-thickness regions). To mitigate this, a set of geometric validity constraints is enforced, so that invalid airfoils are treated via a death-penalty rule as detailed in [subsection 2.4](#).

The constraints, summarized in ([Table 2](#)), are defined for normalized chord coordinates ($x/c, y/c$). Thickness constraints ensure structural feasibility, while curvature constraints (based on the angle between contiguous panels) enforce smoothness on the upper surface to prevent non-physical oscillations. The lower surface is granted higher geometric freedom to allow for the complex curvature commonly associated with supercritical airfoils. Finally, the trailing edge (TE) region is strictly constrained to prevent premature thickness collapse; specifically, the airfoil thickness in the last 12% is enforced to remain above 0.2% until the final 4% of the chord, ensuring a realistic TE wedge angle.

To demonstrate the effectiveness of these constraints in filtering invalid geometries, a discrete sampling of the parametric space was performed using three equidistant values per design variable. [Figure 1](#) visualizes the resulting design envelope, distinguishing between valid and invalid geometries with color-coded boundaries. The results indicate that the 12-parameter CST formulation yields a broad design space capable of representing diverse aerodynamic shapes, while the imposed constraints effectively segre-

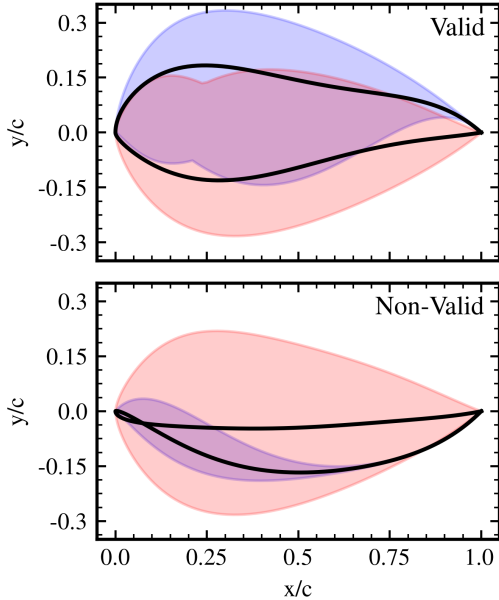


Figure 1: Airfoil parametric space generated using a full factorial combination of three equidistant values within the limits of Table 1. **Left:** The envelope of valid geometries. **Right:** The envelope of geometries discarded by the constraints. The black line indicates the mean surface, while the shaded blue and red regions denote the upper and lower surface boundaries, respectively.

gate degenerate or non-physical curves from the feasible population.

2.2 Numerical Setup

The optimization framework is designed to evaluate aerodynamic performance across varying levels of fidelity. The design problem targets airfoils operating in the incompressible regime at a Reynolds number of $Re = 6 \times 10^6$. Two distinct flight conditions are selected to drive the optimization: a cruise condition at an angle of attack $\alpha = 2^\circ$, representing the primary operational phase, and a take-off condition at $\alpha = 10^\circ$. The latter serves as a critical high-lift case, essential for aircraft configurations where complex high-lift devices may be constrained by weight or mechanical complexity.

The low-fidelity aerodynamic evaluations are performed using XFOIL [56]. XFOIL is a standard tool for airfoil design that couples a high-order inviscid panel method with a fully interactive integral boundary-layer formulation. This viscous-inviscid interaction approach enables rapid prediction of lift and drag with reasonable accuracy in attached-flow conditions [57, 58, 59]. As with other integral boundary-layer approaches, convergence can degrade near stall or for geometries that induce strong separation;

such cases are treated as invalid low-fidelity evaluations within the optimization workflow.

High-fidelity aerodynamic simulations are performed using the open-source CFD toolbox OpenFOAM [60]. The incompressible transient finite-volume solver `pimpleFoam`, which utilizes the PIMPLE algorithm (a combination of PISO and SIMPLE), was employed using a first-order pseudo-transient time scheme designed for steady cases to solve the Reynolds-Averaged Navier-Stokes (RANS) equations. Turbulence was modeled using the $k-\omega$ Shear Stress Transport (SST) model [61], with boundary conditions as detailed in Table 3. The computational domain spans $[-5c, 10c]$ in the streamwise direction and $[-7c, 7c]$ in the vertical direction, normalized by the airfoil chord $c = 1$, and with origin at the airfoil Leading Edge (LE). The domain is discretized using an unstructured triangular-element grid. To resolve flow gradients effectively, local mesh refinement is applied in two zones: a circular region of radius $R = 1.5c$ centered at the LE, and a rectangular wake region extending across $[0, 2.3c] \times [-1.5c, 1.5c]$. To capture boundary layer effects while managing computational cost, an inflation layer with a total height of $0.0352c$ was generated around the airfoil surface. The first cell height was sized to yield an average non-dimensional wall distance of $y^+ \approx 40$, with a maximum of $y^+ \approx 80$. This resolution is consistent with the wall-functions treatment used in the RANS setup. Figure 2 illustrates the mesh topology and refinement zones described above.

To ensure numerical robustness, a mesh convergence study was performed at the most critical condition, corresponding to take-off at $\alpha = 10^\circ$. A total of five mesh refinements were evaluated. The results, presented in Table 4, demonstrate a convergence towards the reference data [62], achieving errors of just 1.26% for C_D and 0.24% for C_L on the finest mesh (the reference values correspond to the average across SST implementations reported in Jespersen et al. [62]). Furthermore, Figure 3 illustrates the excellent agreement of the surface pressure distribution between the reference and the computed results for the finest mesh. Given the inherent geometric complexity of CST-generated airfoils, the finest mesh was selected for the optimization process to minimize discretization errors. The optimization uses the same meshing procedure and refinement settings for all CST geometries; with the automated meshing pipeline, the resulting element count and quality metrics remain consistent across the tested shapes, and mesh-generation failures were not observed in the optimization runs.

2.3 Multi-Fidelity Environment

The primary objective of the multi-fidelity framework is to leverage the computational efficiency of numerous LF simulations while correcting their accuracy using a sparse set of HF data. Kriging (Gaussian Process Regression, GPR) remains widely used in aeronautics, with strategies ranging from simple difference modeling to complex co-Kriging

Table 3: Boundary conditions for high-fidelity RANS simulations. Specific initialization or fixed values are enclosed in brackets $[\cdot]$. ω and k values follow the recommendations by Menter [63]

Field	Inlet	Outlet	Top/Bot.	Airfoil
U	Fixed Value [U_∞]	Inlet/ Outlet [0]	Slip / Zero Grad	No Slip
p	Zero Gradient	Fixed Value [0]	Zero Gradient	Zero Gradient
ω	Fixed Value [0.6]	Zero Gradient	Zero Gradient	ω -Wall Func. [$5.3 \cdot 10^{-8}$]
ν_t	Calculated	Calculated	Calculated	Spalding Wall Func.
k	Fixed Value [$1.1 \cdot 10^{-9}$]	Zero Gradient	Zero Gradient	k_{qr} Wall Function

 Table 4: Mesh convergence study for NACA 0012 airfoil at $\alpha = 10^\circ$ and $Re = 6 \times 10^6$. Values between brackets refer to the absolute relative error compared to the reference [62].

Mesh size	C_D ($\varepsilon_{C_D}, \%$)	C_L ($\varepsilon_{C_L}, \%$)
XFOIL	0.0097700 (21.87)	1.12280 (3.89)
127286	0.0155209 (24.12)	1.04594 (3.22)
508608	0.0124938 (0.09)	1.07599 (0.44)
544552	0.0121113 (3.14)	1.08158 (0.08)
808292	0.0122211 (2.27)	1.07856 (0.20)
1205714	0.0123472 (1.26)	1.07818 (0.23)
Reference [62]	0.0125050	1.08075

approaches that learn scaling factors and bias terms simultaneously. In this study, we adopt an LF-informed regression formulation rather than a hierarchical autoregressive co-Kriging model. The multi-fidelity surrogate predicts a target HF aerodynamic quantity, using the corresponding LF output and the airfoil’s geometric information. This choice is justified by the performance characteristics of XFOIL: while it effectively captures aerodynamic trends in the linear region, it tends to deviate from RANS predictions in non-linear regimes, particularly regarding lift overestimation near separation. Consequently, the goal is to construct a low-fidelity-informed surrogate that maps (Θ, ϕ_{LF}) to an estimate of ϕ_{HF} , providing HF-consistent predictions from LF inputs.

A mapping $f : \phi_{LF} \rightarrow \phi_{HF}$ relying solely on aerodynamic scalars is insufficient. Due to the non-uniqueness in the mapping from LF to HF aerodynamic coefficients, distinct airfoil shapes may yield identical LF performance metrics (e.g., identical efficiency predicted by XFOIL) while exhibiting divergent HF behavior due to complex physics not captured by the panel method (e.g., separation bubbles). To resolve this ambiguity, the geometric parametrization vector Θ is incorporated into the feature space. The corrected HF estimator $\hat{\phi}_{HF}$ is therefore defined as:

$$\hat{\phi}_{HF}(\Theta, \alpha) = f_{GP}(\Theta, \phi_{LF}(\Theta, \alpha)) \quad (1)$$

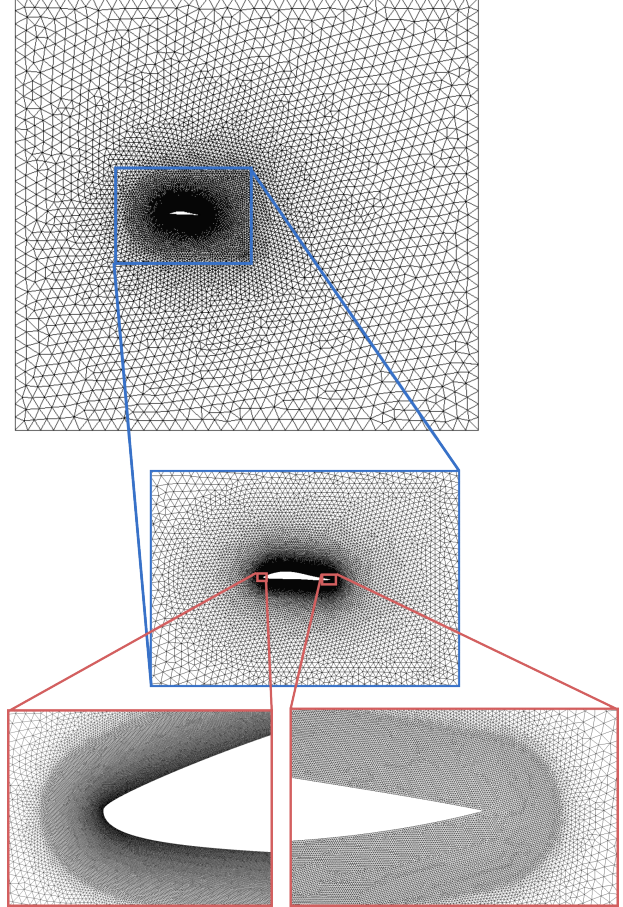


Figure 2: Computational grid for a representative airfoil geometry. The visualization highlights the unstructured domain discretization, the local refinement zones, and the inflation layers resolving the boundary layer at the leading and trailing edges.

where ϕ_{LF} is the coefficient computed by XFOIL, Θ represents the 12 CST parameters, f_{GP} is the trained Gaussian process, and α is the scenario’s angle of attack.

To accurately capture the underlying physics while managing the inherent noise of the low-fidelity solver, a composite kernel is employed. The covariance is modeled as a scaled Radial Basis Function (RBF) kernel, which decouples the signal variance (amplitude) from the length scale (correlation). Furthermore, a white noise kernel is added to the covariance matrix, which captures observation noise in the LF outputs (e.g., convergence and numerical artifacts), thereby separating it from the smooth underlying trend. The resulting kernel function $\psi(x, x')$ is defined as:

$$\psi(x, x') = \sigma_f^2 \cdot \exp\left(-\frac{\|x - x'\|^2}{2l^2}\right) + \sigma_n^2 \delta_{x, x'} \quad (2)$$

where σ_f^2 is the signal variance (amplitude), l is the length-scale parameter governing the smoothness of the correlation, σ_n^2 represents the noise variance, and $\delta_{x, x'}$ is the

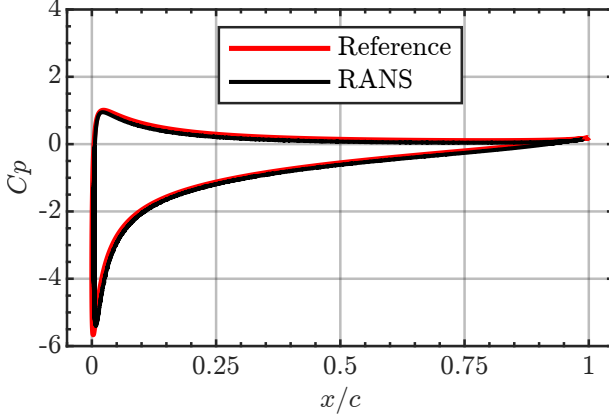


Figure 3: Surface pressure of the finest mesh versus the reference surface pressure, obtained from Jespersen et al. [62].

Kronecker delta function (1 if $x = x'$, 0 otherwise). Hyperparameters (σ_f, l, σ_n) are optimized during the model training phase by maximizing the log-marginal likelihood.

A key element of the proposed framework is the integration of an active learning strategy driven by uncertainty quantification. By exploiting the probabilistic nature of Gaussian Processes, the model provides not only a point prediction but also an estimate of the epistemic uncertainty (prediction variance) at any location in the design space. This capability is leveraged to automatically identify and correct unreliable predictions during the optimization process. A normalized uncertainty metric, the Coefficient of Variation (CV), is defined as the ratio of the predicted standard deviation to the predicted mean ($CV = \sigma_{\phi_{HF}} / \hat{\phi}_{HF}$). Compared with using $\sigma_{\phi_{HF}}$ alone, CV provides a scale-normalized reliability indicator that is comparable across objectives and flight conditions, and it is used here solely to govern fidelity escalation rather than to define an optimization acquisition function. Since ϕ_{HF} remains strictly positive over the explored design space, the normalization does not suffer from near-zero denominators. If this metric exceeds a user-defined threshold κ , the surrogate prediction is deemed insufficiently reliable. In such cases, the candidate is scheduled for HF evaluation. The resulting HF data is then ingested into the training set, and the Kriging model (f_{GP}) is retrained on-the-fly. This mechanism ensures that the surrogate model iteratively refines itself in unexplored or non-linear regions of the design space. Figure 4 illustrates the complete workflow, mapping the parametric vector Θ to the final multi-fidelity prediction, and algorithm 1 contains pseudo-code summarizing the methodology.

Furthermore, the proposed multi-fidelity architecture employs a decoupled modeling strategy, where independent GPR models are assigned to each flight condition (angle of attack α) and aerodynamic coefficient. This decoupling provides a significant advantage over monolithic models: it allows for condition-specific uncertainty thresholds (κ).

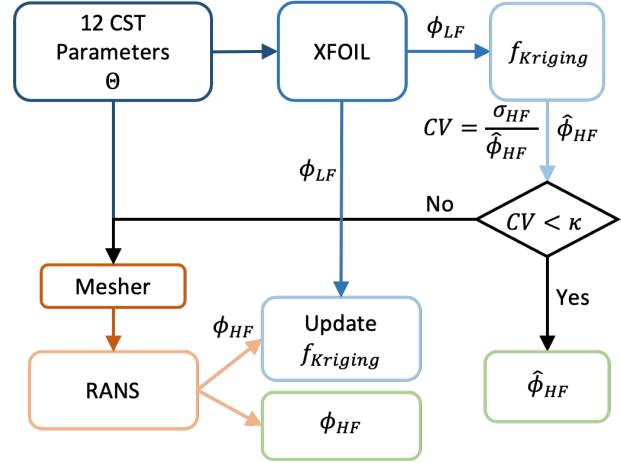


Figure 4: Schematic of the multi-fidelity evaluation workflow. The process accepts a geometric parameter vector Θ , evaluates the low-fidelity physics, and queries the Kriging surrogate. The active learning loop is triggered if the prediction uncertainty CV exceeds the threshold κ , invoking the High-Fidelity solver for model refinement.

Accordingly, each condition-specific model is trained on the subset of airfoils for which the corresponding LF/HF evaluations at that α are available; when an HF call is triggered for a given α , only the dataset and model for that condition are augmented and retrained.

The calibration of the uncertainty thresholds is performed immediately following the initialization phase. Once the initial surrogate baseline is established using the initial training set, a calibration study is conducted using 1000 randomly sampled individuals evaluated via the low-fidelity solver, different from those used for initialization of the optimizer. These samples are then queried against the multi-fidelity models to generate HF estimates and their associated uncertainty metrics (i.e. CV). To balance computational cost with model robustness, the thresholds κ are defined at the 90th percentile of the resulting uncertainty distribution. This criterion limits HF calls to the most uncertain candidates (approximately 10% under the calibration distribution), providing a pragmatic balance between refinement and cost. Other percentile choices are possible and would trade HF budget against surrogate correction aggressiveness; the 90th percentile was selected to keep HF usage bounded while still correcting excursions into uncertain regions. This procedure yielded thresholds of $\kappa_{\alpha=2^\circ} = 0.05$ and $\kappa_{\alpha=10^\circ} = 0.02$, which are held fixed for the remainder of the optimization.

The marked asymmetry between these two thresholds reflects a structural difference in the LF–HF discrepancy across operating conditions. At cruise ($\alpha = 2^\circ$), the target objective is aerodynamic efficiency (L/D), which depends critically on accurate drag prediction. Two factors compound the LF–HF mismatch for this quantity. First, XFOIL’s viscous–inviscid interaction formulation is inherently limited in its ability to predict drag with the same

Algorithm 1: Uncertainty-driven evaluation of an individual.

Require : Design $\Theta^{(i)}$, threshold κ , surrogate GPR, training set \mathcal{D} .

Ensure : $(J^{(i)}, CV^{(i)}, HF^{(i)}, \text{GPR}, \mathcal{D})$.

```

1 Evaluate LF physics  $\phi_{LF}^{(i)}$ 
2 if Solver problem then
3     | death penalty:  $J^{(i)} \leftarrow \infty$ .
4 else
5     | Query surrogate  $(\hat{\phi}_{HF}^{(i)}, \sigma^{(i)}) \leftarrow \text{GPR}(\Theta^{(i)}, \phi_{LF}^{(i)})$ 
6     | Compute uncertainty metric  $CV^{(i)} \leftarrow \sigma^{(i)} / \hat{\phi}_{HF}^{(i)}$ 
7     | if  $CV^{(i)} < \kappa$  then
8         | Assign cost using LF-informed surrogate:
9         |  $J^{(i)} \leftarrow J(\hat{\phi}_{HF}^{(i)})$ 
10    | else
11        | Run HF solver  $\phi_{HF}^{(i)} \leftarrow \text{HF}(\Theta^{(i)})$ 
12        | Assign cost using HF:  $J^{(i)} \leftarrow J(\phi_{HF}^{(i)})$ 
13        | Update training set and retrain:
14        |  $\mathcal{D} \leftarrow \mathcal{D} \cup \{(\Theta^{(i)}, \phi_{LF}^{(i)}, \phi_{HF}^{(i)})\}$ 
15        | Re-train the multi-fidelity model
16        |  $\text{GPR} \leftarrow \text{Train}(\mathcal{D})$ 
17 return  $(J^{(i)}, CV^{(i)}, HF^{(i)}, \text{GPR}, \mathcal{D})$ 
    
```

fidelity as lift, particularly in regimes where pressure recovery and incipient separation influence the drag budget. Second, the two solvers adopt fundamentally different assumptions regarding the boundary-layer state: XFOIL employs an e^N transition model that can predict extended laminar regions and the associated lower skin-friction drag. At cruise, where the drag pressure contribution is not as pronounced, this discrepancy is exacerbated, leading to systematic differences in drag estimation that the surrogate must correct through a more permissive uncertainty threshold. At take-off ($\alpha = 10^\circ$), the strong adverse pressure gradient near the leading edge forces natural transition far upstream, so that both solvers effectively model a predominantly turbulent boundary layer. As a result, the LF–HF agreement for (C_L) at this condition is already strong, and only a tight threshold ($\kappa_{\alpha=10^\circ} = 0.02$) is needed to capture the residual discrepancy. This physical interpretation is consistent with the surrogate validation results presented in section 3, where the RMSRE reduction achieved by the transfer mapping is substantially larger for cruise efficiency than for take-off lift.

2.4 Optimization Problem Formulation

The multi-condition objectives of the study are encapsulated in a single scalar cost function J , which the algorithm seeks to minimize. The design goal is twofold: first, to maximize aerodynamic efficiency ($E = L/D$) at the cruise condition ($\alpha = 2^\circ$); and second, to maximize the lift coefficient (C_L) at the take-off condition ($\alpha = 10^\circ$). The latter

is critical for enhancing operational safety and reducing reliance on complex high-lift devices. Under cruise conditions, directly modeling E yielded optimization trends comparable to using separate surrogate models for C_L and C_D ; however, the latter introduces additional complexity (including uncertainty/error propagation through the ratio) and was therefore not retained in the present implementation.

To formulate this multi-objective maximization problem as a single-objective minimization task, the cost function is defined as the inverse of a weighted sum:

$$J = \frac{1}{0.5 \cdot \hat{E}^{\alpha=2^\circ} + 0.5 \cdot \hat{C}_L^{\alpha=10^\circ} + \varepsilon} \quad (3)$$

where ε is a damping constant, and \hat{E} and \hat{C}_L represent the normalized aerodynamic efficiency and lift coefficient, specifically, $\hat{E}^{\alpha=2^\circ} = E^{\alpha=2^\circ} / \bar{E}_0^{\alpha=2^\circ}$ and $\hat{C}_L^{\alpha=10^\circ} = C_L^{\alpha=10^\circ} / \bar{C}_{L,0}^{\alpha=10^\circ}$, where $\bar{(\cdot)}_0$ denotes the mean over the initial population. Normalization is performed using the mean performance values observed in the initial population. This scaling ensures that both metrics possess comparable magnitudes, justifying the use of equal weighting ($w = 0.5$). The damping constant ε regularizes the reciprocal formulation by limiting fitness amplification when the weighted sum becomes small due to early-iteration surrogate errors or solver outliers. In the present study, $\varepsilon = 10$ was selected pragmatically to moderate selection pressure while preserving the relative ranking of candidates, since the normalized terms remain $\mathcal{O}(1)$ over the explored design space.

The optimization is initialized using Latin Hypercube Sampling (LHS) to ensure a space-filling distribution of the initial population. A total of 100 candidate geometries were sampled and subjected to both low- and high-fidelity simulations. Of these, 83 converged successfully in both solvers, with the non-converging cases attributed to extreme geometric complexities, mesh-generation or solver-convergence issues. These 83 valid individuals constitute the initial population used to train the baseline surrogate models.

2.5 Optimization Framework

The present study addresses a multi-condition airfoil design problem over a 12-parameter CST space, without warm-starting from an existing baseline beyond the parameter bounds and geometric feasibility constraints. A hybrid genetic algorithm, HyGO [55], is employed as the global optimizer for this task. Genetic optimization provides global-search capability, which supports exploration of weakly constrained design spaces, but it can require a large number of evaluations to converge. HyGO addresses this limitation by hybridizing a standard GA with a local-search Downhill Simplex algorithm (DSM) [64] to improve exploitation and accelerate convergence. In HyGO, the CST parameters are encoded using a fixed-

Table 5: Optimization hyperparameters for HyGO

Name	Value	Description
N_b^f	5	Bit number per parameter
N_g	15	Total number of generations
N_{init}	83	Initialization size
N_{explor}^{2-4}	75	Gen. 2 - 4 Exploration size
N_{explor}^{5-15}	50	Gen. 5 - 15 Exploration size
N_T	7	Tournament size
p_T	1	Tournament selection probability
P_c	0.55	Crossover probability
P_m	0.45	Mutation probability
p_m	0.05	Mutation Bit flip Probability
N_e	3	Elitism individuals
d_e	$0.05 \cdot \mathcal{L}$	Elitism minimum distance
$N_{exploit}$	15	Exploitation offspring
N_s	13	Simplex Size

length binary representation (N_b^f bits per parameter) and decoded to continuous values within the bounds in Table 1.

The hyperparameters governing the optimization are reported in Table 5. The HyGO run is limited to a maximum of $N_g = 15$ generations, with an early-stopping criterion triggered when the best objective value does not improve for three consecutive generations. To promote broad exploration of the 12-parameter CST space in the early stages, the exploration population size is set to $N_{explor}^{2-4} = 75$ for Generations 2–4 and reduced to $N_{explor}^{5-15} = 50$ from Generation 5 onward to concentrate computational effort on refinement. The evolutionary selection follows the tournament procedure described in Robledo et al. [55], with crossover and mutation applied with probabilities $P_c = 0.55$ and $P_m = 0.45$ and a bit-flip probability $p_m = 0.05$. The hybridization stage performs local-search exploitation on $N_{exploit} = 15$ candidates per generation using the Downhill Simplex method. These settings were selected pragmatically based on prior HyGO performance on comparable engineering optimization problems and the desired exploration–exploitation trade-off under the available evaluation budget. For further details on the algorithm and its hyperparameters, refer to Robledo et al. [55].

Given the probabilistic nature of the multi-fidelity surrogate and the risk of premature convergence, the standard elitism mechanism was modified to prioritize robustness and diversity. Instead of preserving a single elite individual, three individuals ($N_e = 3$) are propagated to the next generation. However, selecting the top three performers often leads to preserving a cluster of nearly identical solutions, particularly when hybridization with local search methods (DSM) is employed. To mitigate this, a geometric diversity constraint is enforced during the selection of the second and third elites. While the global best individual is always preserved, subsequent elites are selected conditionally. A candidate is only accepted as an elite if it maintains a minimum Euclidean distance of 5% of the

parametric domain’s characteristic length \mathcal{L} (defined as the mean range of the parameters) from any already selected elite. This mechanism ensures the algorithm maintains and propagates distinct potential local minima, preventing the population from collapsing into a single basin of attraction.

Finally, to avoid propagating unvalidated surrogate estimates in the elite set, all elite candidates undergo mandatory high-fidelity (RANS) evaluation before the generation update. This requirement introduces a synchronization challenge within the optimization loop: because the surrogate is retrained whenever new high-fidelity data are acquired, individuals evaluated early in a generation may have fitness values computed under an earlier surrogate state than those evaluated later. A synchronization step is therefore applied to ensure that fitness values used for selection are consistent with the current surrogate model, preventing selection decisions based on stale evaluations.

To address this, a modified evolution procedure is implemented. The generation cycle begins by generating the population using standard Genetic Algorithm operators and hybrid exploitation steps. During this phase, the active learning strategy remains active; any candidate exceeding the uncertainty threshold (κ) triggers an immediate high-fidelity simulation and subsequent model update. Once all candidates have been assigned a fitness value for the current generation, the top three elite candidates are selected and subjected to a mandatory high-fidelity simulation. These results are ingested into the training set, triggering a final model update for the current generation.

Following the multi-fidelity model update, a global re-evaluation is performed to correct for any outdated surrogate states. All individuals in the population that were evaluated solely by the low-fidelity surrogate are re-evaluated against the newly updated model. A critical stability mechanism is enforced at this stage: if a re-evaluated individual violates the uncertainty condition ($CV > \kappa$) under the updated model, it is not required for high-fidelity simulation. Instead, to prevent infinite recursive loops of simulation and model updates and to bound the per-generation HF budget, these candidates are assigned a death penalty ($J = \infty$), effectively removing them from the reproductive pool (the interested reader in death-penalty handling is referred to [65, 55]). Finally, the population is ordered based on the synchronized costs, the elite set is not revised (even if outranked after the re-evaluation) after synchronization within the same generation to avoid infinite iterations, and the standard crossover and mutation operators are applied to the remaining pool to produce the next generation. Algorithm 2 includes a pseudo-code of the procedure for clarity.

The proposed workflow assumes that both the low-fidelity (XFOIL) and high-fidelity (RANS) solvers return converged, physically meaningful outputs. In practice, solver instability and the wide design space enabled by the CST parametrization can lead to non-convergence or invalid solutions. At the low-fidelity level, XFOIL provides explicit warning flags upon failure; whenever such a warning is

Algorithm 2: Modified evolution strategy with uncertainty-triggered fidelity selection and synchronized elitism. The individual evaluation process is described in [algorithm 1](#).

Require : Generation index $g = 1$, maximum generations N_g , elitism size N_e , exploration offspring N_{explore} , exploitation offspring N_{exploit} , uncertainty threshold κ , training set \mathcal{D} , surrogate GPR.

Ensure : Best design Θ^* .

```

1  while not converged and  $g < N_g$  do
    — Exploration stage —
2  Generate  $N_{\text{explore}}$  offspring from  $N_e$  elites using replication/crossover/mutation
3  for  $i \leftarrow 1$  to  $N_{\text{explore}}$  do
4  |  $(J^{(i)}, CV^{(i)}, HF^{(i)}, \text{GPR}, \mathcal{D}) \leftarrow \text{EvaluateIndividual}(\Theta^{(i)}, \kappa, \text{GPR}, \mathcal{D})$ 
    — Synchronization (LF-only individuals) —
5  foreach individual  $j$  evaluated only with GPR in this generation do
6  | Query the updated surrogate  $(\hat{\phi}_{HF}^{(j)}, \sigma^{(j)}) \leftarrow \text{GPR}(\Theta^{(j)}, \phi_{LF}^{(j)})$ 
7  | Re-compute uncertainty metric  $CV^{(j)} \leftarrow \sigma^{(j)} / \hat{\phi}_{HF}^{(j)}$ 
8  | if  $CV^{(j)} < \kappa$  then
9  | | Assign cost using LF-informed surrogate  $J^{(j)} \leftarrow J(\hat{\phi}_{HF}^{(j)})$ 
10 | | else
11 | | death penalty  $J^{(j)} \leftarrow \infty$ 
12 | Sort exploration population by cost:  $\{J_1^g < J_2^g < \dots < J_{N_{\text{explore}}}^g\}$ 
    — Exploitative stage —
13 while  $i < N_{\text{exploit}}$  do
14 | Generate  $N_c$  individuals with DSM operations
15 | foreach DSM-generated candidate per cycle  $j \in \{1, \dots, N_c\}$  do
16 | |  $(J^{(j)}, CV^{(j)}, HF^{(j)}, \text{GPR}, \mathcal{D}) \leftarrow \text{EvaluateIndividual}(\Theta^{(j)}, \kappa, \text{GPR}, \mathcal{D})$ 
17 | | Update number of DSM offspring  $i \leftarrow i + N_c$ 
18 | Sort full population by cost:  $\{J_1^g < J_2^g < \dots < J_{N_{\text{explore}}+N_{\text{exploit}}}^g\}$ 
    — Elitism procedure (HF-validated) —
19 Select the best and  $N_e - 1$  elites using cost and minimum-distance criterion
20 foreach elite candidate  $e \in \{1, \dots, N_e\}$  do
21 | if HF evaluation for  $e$  not available then
22 | | Run HF solver  $\phi_{HF}^{(e)} \leftarrow \text{HF}(\Theta^{(e)})$ 
23 | | Assign cost using HF:  $J^{(e)} \leftarrow J(\phi_{HF}^{(e)})$ 
24 | | Update training set:  $\mathcal{D} \leftarrow \mathcal{D} \cup \{(\Theta^{(e)}, \phi_{LF}^{(e)}, \phi_{HF}^{(e)})\}$ 
25 | | Re-train multi-fidelity model:  $\text{GPR} \leftarrow \text{Train}(\mathcal{D})$ 
26 Re-evaluate LF-only individuals with updated GPR (as Synchronization block) and apply death penalty if
     $CV \geq \kappa$ 
27 Sort population by synchronized costs
28  $g \leftarrow g + 1$ 
29 return  $\Theta^* = \arg \min_{\Theta} J(\Theta)$ 
    
```

triggered, the corresponding individual is assigned a death penalty ($J = \infty$) before the uncertainty evaluation, ensuring that it is immediately discarded by the optimizer. This choice introduces a bias against regions where the LF model fails, but it is acceptable here because the target operating conditions ($\alpha = 2^\circ$ cruise and $\alpha = 10^\circ$ take-off at $\text{Re} = 6 \times 10^6$) are not intended to explore deep-stall behavior; designs that systematically trigger XFOIL failure

typically correspond to strongly separated regimes outside the validity range of the LF solver and outside the intended mission envelope. The alternative of directly evaluating the HF in such cases introduces an uncontrolled triggering mechanism that may easily overflow the simulation budget without providing meaningful information. An analogous screening is applied to high-fidelity evaluations. A high-fidelity result is considered admissible only if all

of the following conditions are satisfied: (i) the simulation reaches the prescribed maximum number of iterations without divergence; (ii) over the last 2,000 iteration steps, the standard deviations of C_L and C_D , normalized by their respective means, are below 0.05; and (iii) both C_L and C_D remain positive to exclude non-physical solver outputs. This screening procedure increases robustness by ensuring that only converged, physically consistent high-fidelity outputs are used to evaluate the cost function and update the surrogate models.

Finally, the framework incorporates a geometric validity check based on the constraints defined in subsection 2.1. Leveraging HyGO’s feasibility handling mechanism, individuals flagged as invalid are first subject to regeneration attempts via genetic operators. If a candidate fails to meet the validity criteria after a maximum number of regeneration attempts (1000 in this work), it is discarded. This strategy significantly enhances computational efficiency by preventing the allocation of simulation resources to *a priori* infeasible designs, effectively confining the search to the productive regions of the parametric space.

3 Results

The optimization campaign evaluated a total of 1042 individuals across 15 generations. The evolution of the cost function is depicted in Figure 5. The best individual was effectively achieved by generation 5 (marked by \star), followed by a plateau in performance till generation 15, highlighting convergence. The results demonstrate that the algorithm successfully refines the initial population generated via Latin Hypercube Sampling. Notably, the hybrid exploitation mechanism (DSM) played a critical role in the early stages, producing several high-performing individuals in the first two generations that significantly accelerated convergence toward the best-found design.

The quantitative outcomes of the optimization campaign are summarized in Table 6. A direct comparison between the best individual from the first generation (which notably already benefited from local search exploitation) and the final optimized geometry highlights the substantial performance improvements achievable through the optimization process. The method yielded a 20.75% increase in $C_L^{\alpha=10^\circ}$ and a 41.05% improvement in $E^{\alpha=2^\circ}$. Physically, the final take-off lift $C_L^{\alpha=10^\circ} = 1.833$ is high for a single-element airfoil at the specified operating condition. Such lift levels are typically associated with strongly cambered geometries and often accompanied by a significant drag penalty due to increased pressure drag and thicker boundary layers. In the present case, however, the configuration also exhibits a high aerodynamic efficiency $E^{\alpha=2^\circ} = 111.43$ despite the pronounced camber of the optimized airfoil. This indicates that the optimization procedure has identified a pressure distribution that enhances lift generation while maintaining a comparatively favorable recovery in the aft region, thereby limiting the drag increase that would normally accompany such high lift coefficients. Regarding geometry

Table 6: Optimization results for the 12-parameter CST representation, including the aerodynamic performance metrics. Results for the best individual after the first generation and the overall best reached after the fifth generation.

Variable	Gen. 1	Gen. 5–15
$C_L^{\alpha=10^\circ}$	1.518	1.833 (20.75% \uparrow)
$E^{\alpha=2^\circ}$	79	111.43 (41.05% \uparrow)
θ_1	0.43961	0.27546
θ_2	0.29592	0.12594
θ_3	0.66546	0.53639
θ_4	0.05585	0.17579
θ_5	0.34700	0.34700
θ_6	0.09677	-0.16129
θ_7	-0.11924	-0.16335
θ_8	-0.27301	-0.16790
θ_9	-0.00118	0.10869
θ_{10}	0.04885	0.40348
θ_{11}	-0.07258	0.15619
θ_{12}	0.08158	-0.03860

representation, the final design reveals that the CST parameters converged to intermediate values, well within the user-defined bounds. This interior solution suggests that the parametric envelope was sufficiently broad.

The optimized geometric topology is depicted in Figure 6 (marked by the blue star \star). The resulting shape is non-standard within the sampled envelope, characterized by pronounced aft-loading and extreme camber peaking near $x/c \approx 0.5$. This aft-camber distribution is efficient for lift generation but introduces a geometric inflection on the lower surface. Consequently, the aft region of the pressure side is subjected to a steep adverse pressure gradient, with risk of flow separation at low angles of attack (such as the cruise condition, $\alpha = 2^\circ$). Furthermore, the thickness distribution is noticeably decoupled from the camber; the maximum thickness is concentrated in the forward characteristic length, while the curvature drives the aft section. Notably, the upper surface exhibits a flattened, quasi-linear region immediately downstream of the leading edge. This geometry aligns the surface almost parallel to the local inflow at $\alpha = 10^\circ$, effectively delaying the suction peak, broadening the suction distribution, and delaying separation onset.

The evolution of the specific aerodynamic objectives is detailed in Figure 5. Rapid improvements in both metrics are observed in the initial generations. Interestingly, a subset of early individuals (corresponding to generations 2-3) exhibits higher lift coefficients at take-off than the final design. Analysis of the representative geometric profiles (bottom of Figure 6) reveals that this high lift was primarily driven by increased airfoil thickness. However, excessive thickness incurs a substantial drag penalty, detrimental to the cruise efficiency objective. Consequently, later generations move toward a geometric compromise, balancing reduced thickness with optimized camber to maximize the

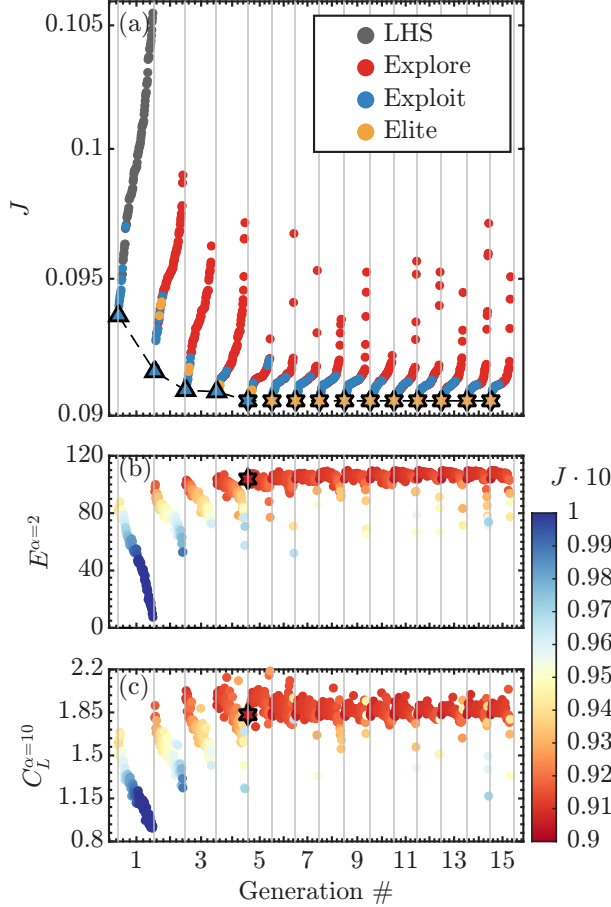


Figure 5: Evolution of the optimization campaign and aerodynamic objectives. (a) Cost-function convergence (J) over 15 generations, with individuals labeled by generation method (LHS, exploration, exploitation, elitism); symbols show the best design in generations 1–4 (Δ) and the overall best individual (\star). (b) Scatter of cruise efficiency ($E^{\alpha=2^\circ}$) and (c) take-off lift ($C_L^{\alpha=10^\circ}$) over 15 generations, color-coded by J , with the overall best individual marked by a star.

composite objective function. This trend is visually evident in the optimized profiles of the first five generations (top-left inset), where the geometry progressively evolves from thick, high-lift shapes to thinner, more cambered designs that sustain lift while minimizing drag.

The strong alignment between the two aerodynamic objectives over much of the sampled design space is corroborated in Figure 7, which shows an approximately linear trend across the majority of evaluated candidates. The dashed curves (---) represent iso-contours of the composite cost J in the ($C_L^{\alpha=10^\circ}$, $E^{\alpha=2^\circ}$) plane, obtained by evaluating J on a grid of objective values; they are shown as a visual reference for the direction of decreasing cost. Over most of the explored region, increases in take-off lift ($C_L^{\alpha=10^\circ}$) tend to be accompanied by increases in cruise ef-

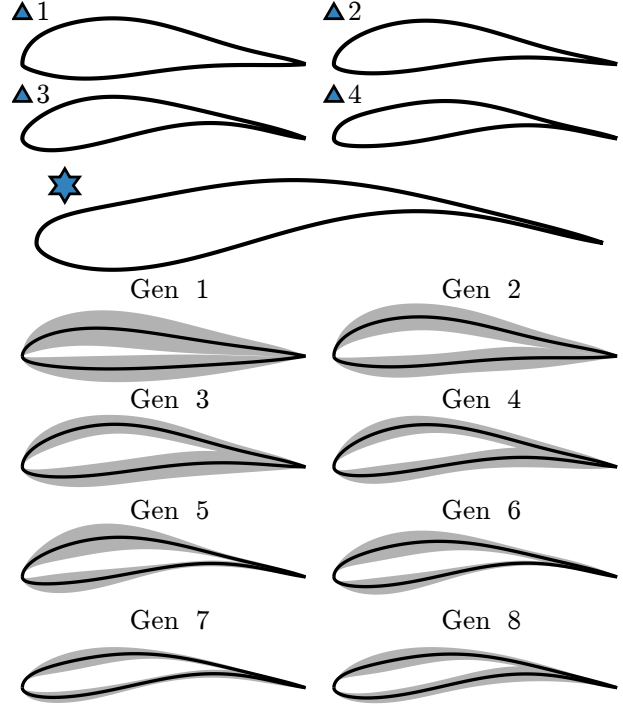


Figure 6: Geometric evolution of the optimized airfoils. Top rows: best individuals from Generations 1–4, marked by triangles (Δ) and colored by their generation operator as in Figure 5. The final best (Generation 5) is shown in the third row, highlighted by a star (\star with the same color convention). Bottom rows: population statistics for Generations 1–8, showing the mean airfoil (solid black line (—)) over the grey envelope of all sampled geometries.

iciency ($E^{\alpha=2^\circ}$), indicating that, within the imposed CST bounds and feasibility constraints, early improvements are only weakly conflicting.

However, this trend breaks down in the upper-right quadrant, where the highest-performing individuals reside, and a distinct Pareto front becomes apparent (marked by a solid black line (—)). This region highlights the local trade-off between further lift gains at take-off and efficiency retention at cruise, consistent with increasing drag sensitivity at high-lift geometries. The bottom half of Figure 7 displays 12 of the 23 Pareto-optimal airfoils and shows smooth, gradual shape transitions along the front. In line with the trends observed in Figure 6, the high- C_L end of the front (green markers \bullet) is dominated by thicker profiles, whereas intermediate Pareto solutions (purple markers \bullet) shift toward increased camber and reduced leading-edge radius.

Notably, the evaluated set does not contain solutions combining high E with low C_L , or vice-versa. This absence is consistent with the fixed-weight scalarization and feasibility constraints: designs with reduced take-off lift are strongly disfavored by the composite objective, so the search concentrates on regions where efficiency gains are

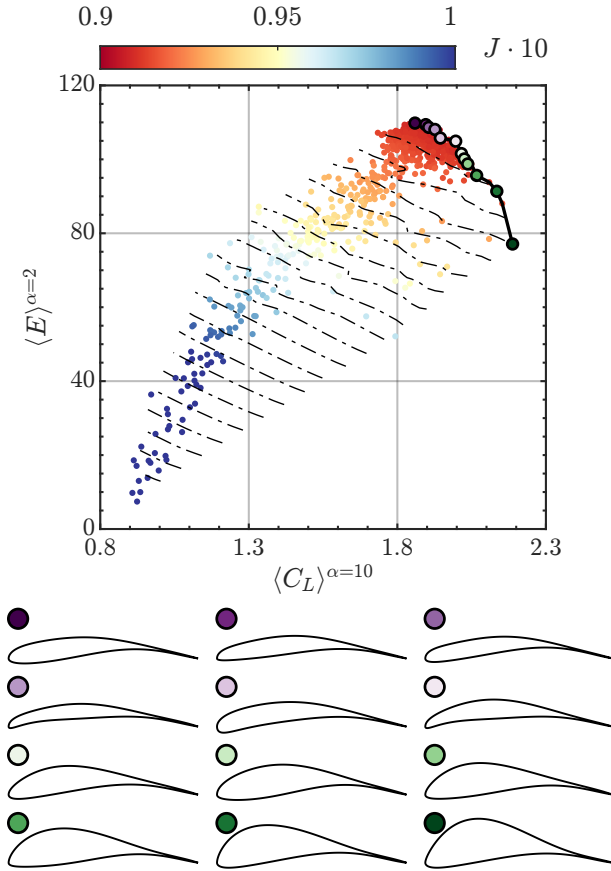


Figure 7: Composite objective analysis. Top: objective space showing the trade-off between cruise efficiency ($E^{\alpha=2^\circ}$) and take-off lift ($C_L^{\alpha=10^\circ}$), with points colored by cost (J) and the Pareto front indicated by a solid black line. Bottom: airfoil geometries along the Pareto front, color-coded to match their locations on the front in the top panel.

achieved without sacrificing $C_L^{\alpha=10^\circ}$. In addition, maximizing $E^{\alpha=2^\circ} = L/D$ alone does not necessarily promote very low-lift geometries, since E depends on the coupled behavior of lift and drag rather than on drag minimization in isolation.

Figure 8 and Figure 9 assess the predictive performance of the proposed LF-informed surrogate. In both figures, the HF reference values are compared against the LF outputs and the surrogate predictions (identified by subindex *pred*) evaluated immediately before assimilating the corresponding HF samples into the model update. This pre-update evaluation avoids optimistic “in-sample” assessment and isolates the effect of the transfer mapping on newly acquired HF points.

For the cruise condition ($\alpha = 2^\circ$) shown in Figure 8, XFOIL exhibits a systematic bias in aerodynamic efficiency, yielding LF values that frequently exceed the HF range encountered in the optimization. This behavior is consistent with the sensitivity of E to drag prediction and

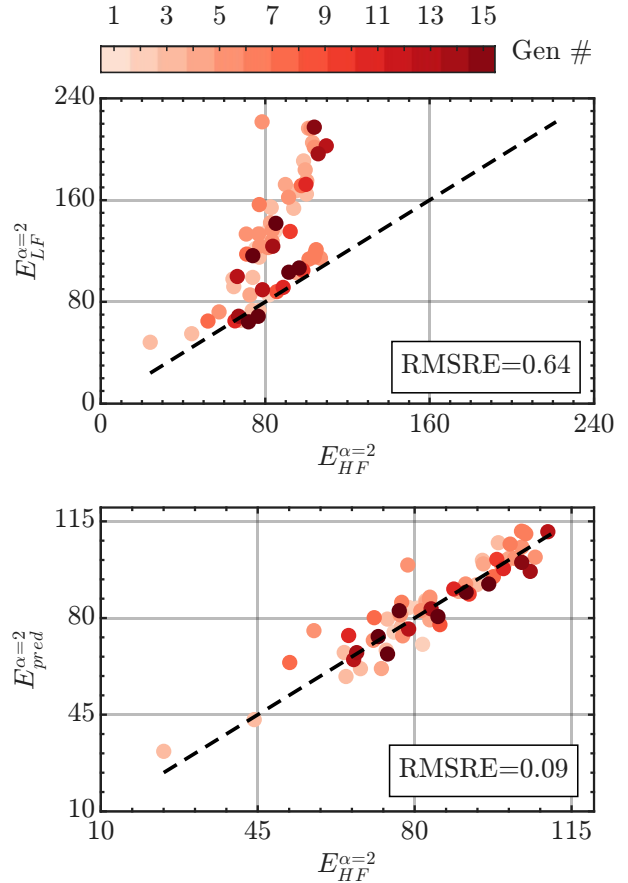


Figure 8: Surrogate validation for the cruise condition ($\alpha = 2^\circ$). Top: HF reference versus LF output (XFOIL). Bottom: HF reference versus LF-informed surrogate prediction evaluated before assimilating the corresponding HF sample (pre-update). Points are colored by generation of acquisition; the dashed line indicates perfect agreement.

with the known limitations of viscous–inviscid approaches in regimes where drag is influenced by separation-related mechanisms. The Kriging-based transfer mapping substantially reduces this bias and the associated scatter, bringing the predictions closer to the identity line. Quantitatively, the root mean squared relative error (RMSRE), computed on each newly acquired HF point before its assimilation and then aggregated across generations, decreases from 0.64 (LF) to 0.09 (pred), i.e., an improvement by approximately a factor of seven. Additionally, the generation-based color coding indicates that later acquisitions tend to concentrate closer to the identity line, which is consistent with progressive local correction of the LF–HF mapping along the optimizer trajectory as additional HF samples are assimilated.

For the take-off condition ($\alpha = 10^\circ$) in Figure 9, the LF–HF agreement for C_L is already strong, and the transfer surrogate primarily reduces residual dispersion. The RMSRE decreases from 0.06 (LF) to 0.01 (pred), indicating that only a modest correction is required for C_L at this

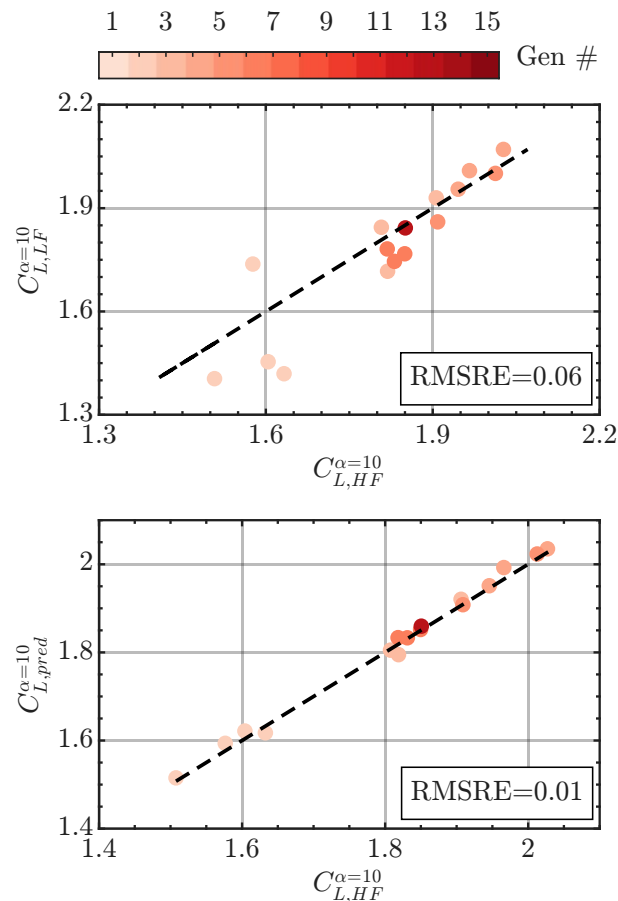


Figure 9: Surrogate validation for the take-off condition ($\alpha = 10^\circ$). Top: HF reference versus LF output (XFOIL). Bottom: HF reference versus LF-informed surrogate prediction evaluated before assimilating the corresponding HF sample (pre-update). Points are colored by generation of acquisition; the dashed line indicates perfect agreement.

condition. Consistent with this, most late-generation HF evaluations are expected to originate from the mandatory HF validation of elite individuals, whereas uncertainty-triggered escalation is comparatively limited for the C_L model.

This behavior in later generations is further quantified by the number of HF simulations per generation, presented in Figure 10. Although the best design is first identified by Generation 5 and the campaign satisfies the HyGO convergence criterion by Generation 8 (no improvement over three consecutive generations), the run was intentionally continued to Generation 15. This extended phase isolates the effect of online surrogate refinement and illustrates how uncertainty-triggered HF escalation diminishes as the LF-informed transfer models become better calibrated in the regions visited by the optimizer, illustrated in the bottom panel of Figure 10 by the correlation between the cumulative simulations and the minimal cost evolution.

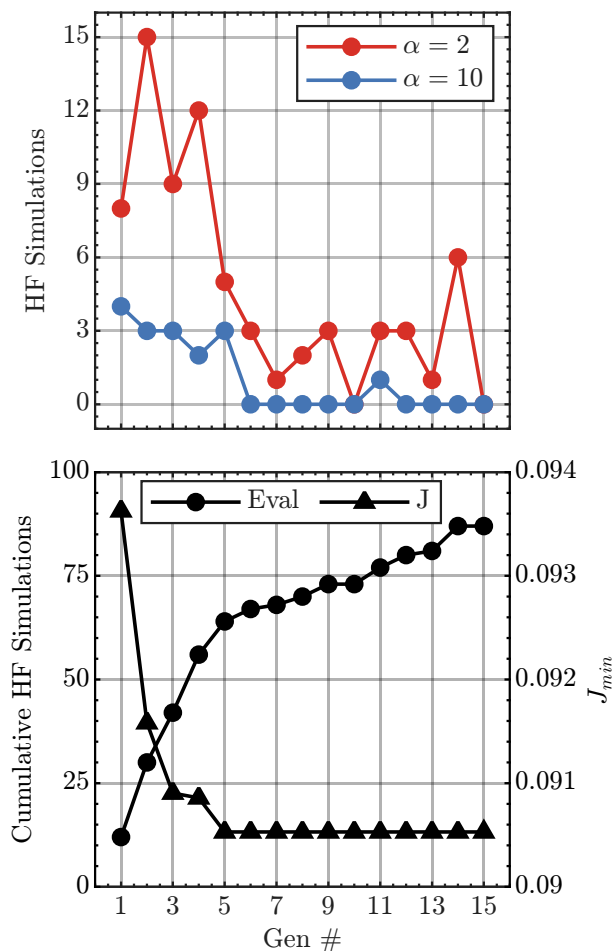


Figure 10: High-fidelity budget per generation. Top: Number of HF simulations executed at each flight condition as a function of generation. Bottom: Cumulative number of HF simulations for both conditions and best cost per generation.

The resulting HF budget exhibits a marked asymmetry between operating conditions. For the cruise condition ($\alpha = 2^\circ$), a comparatively large number of HF calls is required in early generations (e.g., in Generation 1, 8 of the 20 exploitation candidates exceed the uncertainty threshold). Exploration candidates in this phase do not trigger additional HF evaluations, since they are drawn from the initial LHS set already evaluated with RANS. The sustained need for HF updates at $\alpha = 2^\circ$ is consistent with the greater difficulty of transferring efficiency $E = L/D$, which is highly sensitive to drag prediction and therefore amplifies LF–HF discrepancies. In contrast, for the take-off condition ($\alpha = 10^\circ$), the LF–HF agreement for C_L is strong and uncertainty-triggered escalation rapidly vanishes.

Overall, the campaign executed 154 and 99 HF evaluations at $\alpha = 2^\circ$ and $\alpha = 10^\circ$, respectively, including the initial set of 83 geometries evaluated directly at high fidelity.

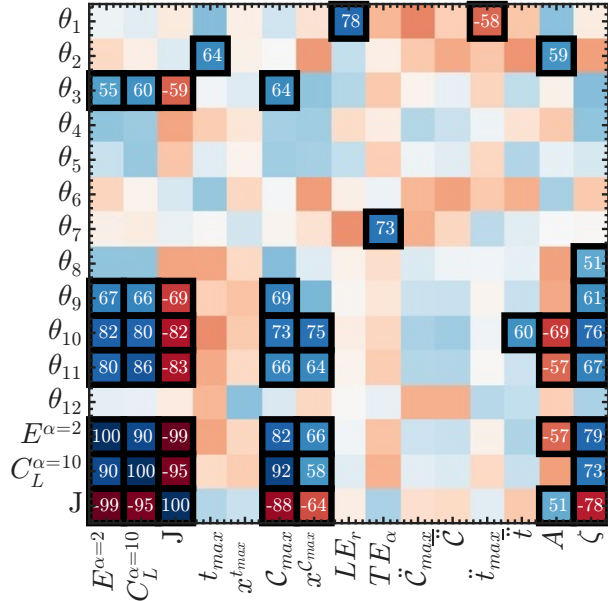


Figure 11: Pearson correlation matrix between CST design parameters (θ_{1-12}), extracted geometric descriptors, and aerodynamic quantities ($E^{\alpha=2^\circ}$, $C_L^{\alpha=10^\circ}$, J). Colors indicate correlation magnitude and sign; boxed entries highlight correlations with $|\rho| \geq 0.5$. Correlations are reported to support the interpretability of dominant geometric drivers, noting that they reflect linear associations rather than causal effects.

Using average wall-clock runtimes of approximately 1.0 h ($\alpha = 2^\circ$) and 1.5 h ($\alpha = 10^\circ$) per simulation, this corresponds to ≈ 302.5 node-hours (207.5 node-hours mandatory for initialization) on a 32-core node (i.e., $\approx 9,680$ core-hours). For reference, an all-HF evaluation strategy that simulated every candidate at both operating points would scale approximately with the total number of evaluated individuals (1042 in this study) and would therefore be substantially more expensive (83,360 node-hours on a 32-core node, as for this study).

While CST offers a compact and flexible parameterization, the physical role of individual coefficients is not immediately interpretable. To relate design variables to aerodynamic behavior, a set of geometric descriptors was extracted for each airfoil: maximum thickness and its location (t_{max} , $x_{t_{max}}$), maximum camber and its location (C_{max} , $x_{C_{max}}$), leading-edge radius (LE_r), trailing-edge angle (TE_{α}), and peak/average curvature for both camber (\bar{C}_{max} , \bar{C}) and thickness (\bar{t}_{max} , \bar{t}). A Pearson correlation analysis between the CST parameters (θ), geometric metrics, and aerodynamic cost values (J , E , C_L) is shown in Figure 11. The dominant correlations indicate that performance variations (E , C_L , and the aggregate cost J) are primarily associated with camber-related features. Both the maximum camber magnitude (C_{max}) and its chordwise position ($x_{C_{max}}$) exhibit a strong positive correlation with the aerodynamic performance. This aligns with fun-

damental aerodynamic theory, identifying camber as the primary mechanism for lift maximization, a trend clearly reflected in the high- C_L peak observed in the optimization history and the Pareto front structure. Conversely, thickness-related measures (e.g., enclosed area A) correlate negatively with E , consistent with the tendency of the optimizer to reduce thickness in order to mitigate drag penalties at cruise. These trends provide an interpretable link between the Pareto-front geometry families discussed previously and the scalar objective driving selection.

A useful composite descriptor is the asymmetry ratio $\zeta = C_{max}/t_{max}$, which compactly summarizes the relative dominance of camber over thickness. The observed correlation of ζ with the aerodynamic objectives indicates that high-performing designs in this campaign tend to increase camber while keeping thickness moderate, consistent with the efficiency-driven penalty of excessive thickness at cruise. At the parameter level, θ_{9-11} exhibit the strongest linear associations with the dominant geometric descriptors, indicating that these coefficients govern much of the performance-relevant variability within the chosen CST bounds. In contrast, θ_3 shows a more selective influence, correlating primarily with camber-related features. The remaining CST coefficients display weaker correlations with the cost function, suggesting a lower first-order sensitivity for the specific operating conditions and objective definition considered here.

To provide physical insight into the optimization trends, the pressure coefficient (C_p) distributions for all evaluated individuals are summarized in Figure 12 and Figure 13 top panels using an unwrapped representation, where each row corresponds to one individual and the chordwise coordinate is mapped along the horizontal axis. This visualization highlights that the two operating points promote distinct loading strategies. At cruise ($\alpha = 2^\circ$, Figure 12), improvements in E are associated with a redistribution of suction and a moderation of pressure recovery, which is consistent with reducing drag penalties linked to adverse pressure gradients and separation sensitivity. At take-off ($\alpha = 10^\circ$, Figure 13), the optimization favors higher integrated loading, achieved by strengthening the suction-side depression and increasing pressure-side loading while maintaining a pressure recovery compatible with attached flow. Together, these trends illustrate the coupled compromise enforced by the composite objective across the two conditions.

The bottom panels of Figure 12 and Figure 13 compare representative C_p profiles at Generation 1 and at Generation 8 (after the best design has stabilized under the HyGO stopping criterion). For cruise ($\alpha = 2^\circ$, Figure 12), the final design exhibits a more front-to-mid-chord distributed loading than the early-generation best candidate. In particular, the suction-side profile shows a pronounced leading-edge depression followed by an extended region of relatively weak recovery up to approximately mid-chord, yielding a sustained pressure difference ($C_{p,\ell} - C_{p,u}$) over the fore-mid chord. This smoother recovery is consistent with limiting mid-chord adverse-pressure-gradient severity in a highly

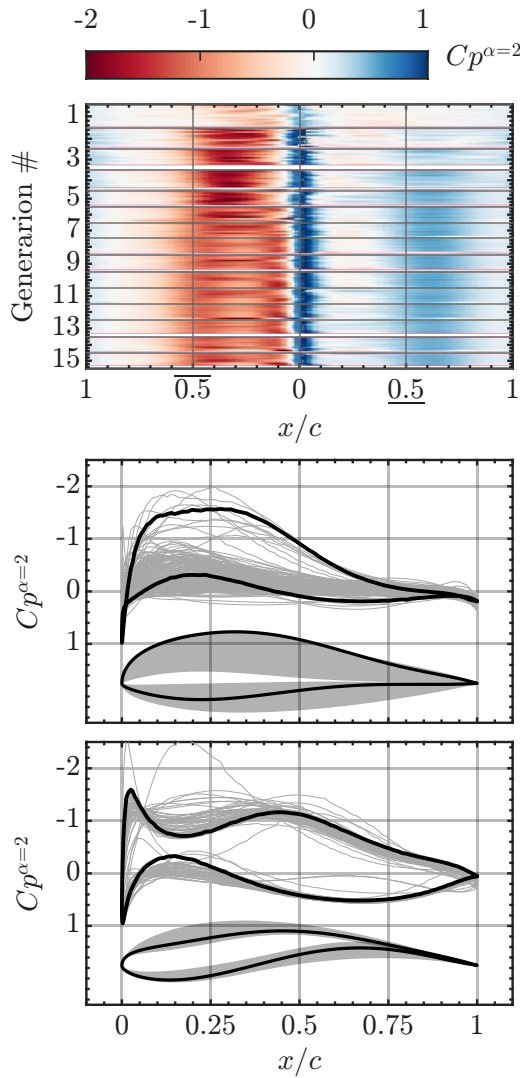


Figure 12: Aerodynamic pressure analysis and evolutionary trends at cruise ($\alpha = 2^\circ$). Top: unwrapped $C_p(x/c)$ map for all evaluated individuals (each row corresponds to one airfoil). Middle: Generation 1 population statistics showing the geometric envelope (■) and the best individual (—), with corresponding C_p profiles. Bottom: analogous results for Generation 8, illustrating population concentration and the C_p signature of the final best design after HyGO's convergence.

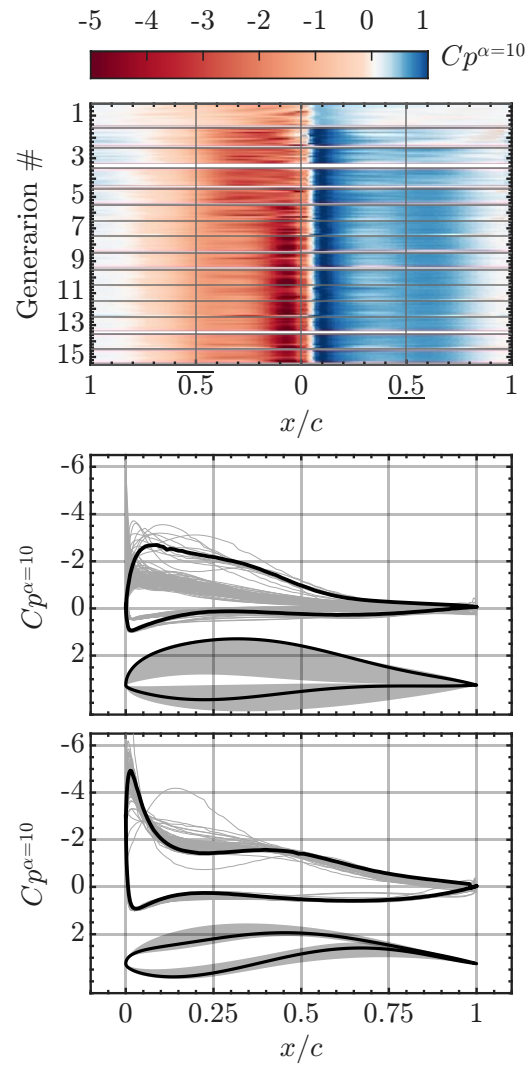


Figure 13: Aerodynamic pressure analysis and evolutionary trends at take-off ($\alpha = 10^\circ$). Top: unwrapped $C_p(x/c)$ map for all evaluated individuals (each row corresponds to one airfoil). Middle: Generation 1 population statistics showing the geometric envelope (■) and the best individual (—), with corresponding C_p profiles. Bottom: analogous results for Generation 8, illustrating population concentration and the C_p signature of the final best design after HyGO's convergence.

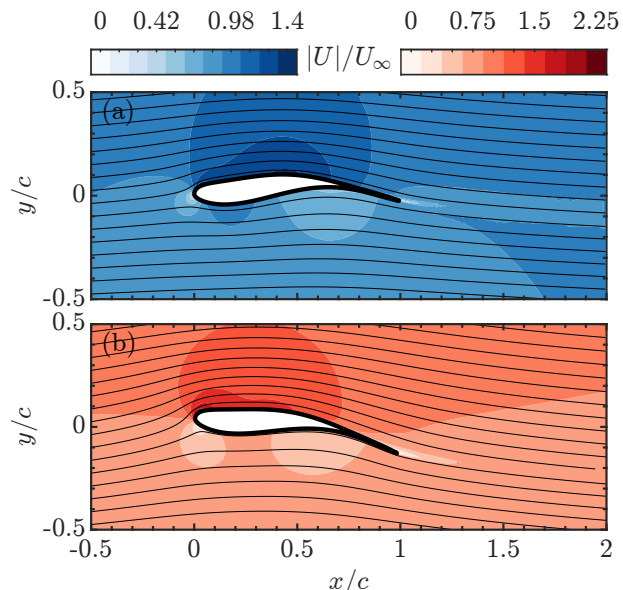


Figure 14: RANS flow-field visualization for the optimized airfoil at (a) cruise, $\alpha = 2^\circ$, and (b) take-off, $\alpha = 10^\circ$, at $Re = 6 \times 10^6$. Contours show the normalized velocity magnitude $|U|/U_\infty$, and black streamlines depict the mean flow topology. The absence of streamline detachment and of extended low-speed recirculation regions over either surface indicates predominantly attached flow for the optimized design at both operating points.

cambered configuration, which is favorable for maintaining attachment and controlling drag. By contrast, the best Generation 1 profile is more characteristic of thickness-driven improvement, with a milder suction peak and a more conservative chordwise evolution of C_p , consistent with the early tendency of the optimizer to exploit thickness increases to raise aerodynamic performance.

At take-off ($\alpha = 10^\circ$, Figure 13), early improvements similarly increase the pressure difference through a combination of stronger suction-side depression and increased pressure-side loading, consistent with lift augmentation. The final best design, however, shifts the emphasis toward camber redistribution at moderate thickness: the selected C_p profile combines a strong leading-edge suction peak with an extended region of comparatively gentle recovery on the suction side, reducing recovery steepness around mid-chord ($x/c \approx 0.5$) where separation onset is typically sensitive. Overall, the population-level maps and the representative profiles support the transition inferred from the Pareto and correlation analyses: coarse thickness variation dominates early exploration, whereas later improvements are achieved primarily through camber shaping and suction redistribution subject to separation-aware pressure recovery constraints.

Figure 14 complements the C_p -based interpretation by providing a qualitative view of the near-body flow for the final optimized airfoil at the two operating points. At $\alpha = 2^\circ$,

the velocity field remains smooth around the leading edge and through the aft region, with streamlines following the suction-side curvature without visible separation, supporting the conclusion that the efficiency gains are achieved through load redistribution and controlled recovery rather than through operating near a separated state. At $\alpha = 10^\circ$, the field shows the expected acceleration over the suction side associated with the high- C_L solution while preserving attached streamlines, indicating that the final geometry sustains the required lift through increased suction and favorable recovery without inducing large-scale separation. Given the 2D RANS context, these visualizations should be interpreted as qualitative evidence of attached/fully separated behavior (rather than a definitive characterization of transitional or small laminar separation bubbles), but they are consistent with the solver-admissibility checks and with the “separation-aware” recovery trends previously inferred from the population C_p evolution.

4 Conclusions

This work presented an active multi-fidelity framework for airfoil shape optimization that combines inexpensive low-fidelity evaluations from XFOIL with sparse, computationally intensive high-fidelity RANS simulations. A low-fidelity-informed Gaussian process regressor was used to map geometric variables and low-fidelity aerodynamic outputs to high-fidelity performance metrics, thereby mitigating systematic low-fidelity biases and providing predictive uncertainty estimates that can be exploited during the search.

An uncertainty-triggered refinement strategy was introduced to adaptively select candidates for high-fidelity evaluation, concentrating computational effort in regions where the surrogate is insufficiently reliable. By enforcing a prescribed uncertainty threshold on surrogate-based predictions and iteratively assimilating newly acquired high-fidelity data, the surrogate accuracy is progressively improved in the portions of the design space explored by the optimizer, particularly in the vicinity of the identified minima. The condition-wise decoupling of surrogate models further enables multi-point optimization without requiring high-fidelity evaluation across the full operating set when uncertainty is localized to a subset of conditions.

The framework was coupled with HyGO, a hybrid genetic algorithm, to retain the global search capabilities of evolutionary optimization while promoting model refinement. To limit the accumulation and propagation of surrogate-induced errors, a modified elitism strategy was proposed in which elite candidates are systematically validated using the high-fidelity solver. The resulting high-fidelity data are used to update the surrogate and to synchronize the population costs before reproduction, improving the reliability of the information presented to the optimizer. A diversity constraint on elite selection further prevents redundant high-fidelity evaluations and mitigates prema-

ture concentration of the search around a single basin of attraction.

The proposed methodology was demonstrated on a two-point optimization representative of cruise ($\alpha = 2^\circ$) and take-off ($\alpha = 10^\circ$) at $Re = 6 \times 10^6$. Under these conditions, the optimized design achieved simultaneous improvements of 20.75% in take-off lift coefficient ($C_L^{\alpha=10^\circ}$) and 41.05% in cruise aerodynamic efficiency ($E^{\alpha=2^\circ}$). In addition, the pre-update validation results confirm that the LF-informed transfer surrogate substantially reduces the LF–HF discrepancy for the drag-sensitive efficiency objective while requiring only limited correction for C_L at take-off, which is consistent with the observed asymmetry in uncertainty-triggered high-fidelity calls across operating points.

Overall, the main contribution of this study is an optimization-embedded active multi-fidelity strategy in which (i) high-fidelity escalation is governed by predictive uncertainty at the candidate level rather than by a fixed per-generation budget, and (ii) synchronization mechanisms (elite validation, population re-evaluation, and diversity-aware elitism) are used to control surrogate-induced drift within an evolutionary optimizer. The conclusions drawn in this work remain conditional on the assumptions inherent to the chosen solvers and problem formulation (RANS modeling, CST parametrization, and the specific operating points and constraints considered). Nevertheless, the results support the use of online-refined multi-fidelity surrogates coupled with global, model-free optimizers for multi-point aerodynamic shape optimization. Future work will focus on extending the framework to richer fidelity hierarchies, broader operating envelopes and constraint sets, and three-dimensional and multidisciplinary configurations.

Funding Sources

This work has been supported by the TIFON project, ref. PLEC2023-010251/MCIN/AEI/10.13039/501100011033, funded by the Spanish State Research Agency. Oriol Lehmkuhl has been partially supported by a Ramon y Cajal postdoctoral contract (Ref: RYC2018-025949-I). We also acknowledge the Barcelona Supercomputing Center for awarding us access to the MareNostrum V machine based in Barcelona, Spain.

Code and Data availability

The framework will be made openly available to the research and engineering community after the review process is finished, under the MIT license, including source code, documentation, and ready-to-use examples.

References

[1] A. Jameson, Aerodynamic design via control theory, *Journal of scientific computing* (1988).

[2] J. Reuther, A. Jameson, J. Farmer, L. Martinelli, D. Saunders, Aerodynamic shape optimization of complex aircraft configurations via an adjoint formulation, in: 34th aerospace sciences meeting and exhibit, 1996, p. 94.

[3] J. P. Slotnick, A. Khodadoust, J. Alonso, D. Darmofal, W. Gropp, E. Lurie, D. J. Mavriplis, CFD vision 2030 study: a path to revolutionary computational aerosciences, Technical Report No. NF1676L-18332, NASA, 2014.

[4] R. Yondo, E. Andrés, E. Valero, A review on design of experiments and surrogate models in aircraft real-time and many-query aerodynamic analyses, *Progress in aerospace sciences* (2018).

[5] Z.-H. Han, S. Görtz, Hierarchical kriging model for variable-fidelity surrogate modeling, *AIAA journal* 50 (2012) 1885–1896.

[6] J. Nagawkar, L. T. Leifsson, X. Du, Applications of polynomial chaos-based cokriging to aerodynamic design optimization benchmark problems, in: *AIAA Scitech 2020 Forum*, 2020, p. 0542.

[7] J. Laurenceau, P. Sagaut, Building efficient response surfaces of aerodynamic functions with kriging and cokriging, *AIAA journal* (2008).

[8] Z.-H. Han, Y. Zhang, C.-X. Song, K.-S. Zhang, Weighted gradient-enhanced kriging for high-dimensional surrogate modeling and design optimization, *Aiaa Journal* (2017).

[9] M. A. Bouhlel, J. R. Martins, Gradient-enhanced kriging for high-dimensional problems, *Engineering with Computers* (2019).

[10] M. A. Bouhlel, N. Bartoli, A. Otsmane, J. Morlier, Improving kriging surrogates of high-dimensional design models by partial least squares dimension reduction, *Structural and Multidisciplinary Optimization* (2016).

[11] M.-Y. Wu, X.-Y. Yuan, Z.-H. Chen, W.-T. Wu, Y. Hua, N. Aubry, Airfoil shape optimization using genetic algorithm coupled deep neural networks, *Physics of Fluids* 35 (2023).

[12] V. Esfahanian, M. J. Izadi, H. Bashi, M. Ansari, A. Tavakoli, M. Kordi, Aerodynamic shape optimization of gas turbines: a deep learning surrogate model approach, *Structural and Multidisciplinary Optimization* 67 (2023). doi:10.1007/s00158-023-03703-9.

[13] M. Raissi, P. Perdikaris, G. E. Karniadakis, Physics-informed neural networks: A deep learning framework for solving forward and inverse problems involving nonlinear partial differential equations, *Journal of Computational physics* (2019).

[14] K. Shukla, V. Oommen, A. Peyvan, M. Penwarden, L. Bravo, A. Ghoshal, R. M. Kirby, G. E. Karniadakis, Deep neural operators can serve as accurate surrogates for shape optimization: a case study for airfoils, *arXiv* (2023).

- [15] L. Lu, P. Jin, G. Pang, Z. Zhang, G. E. Karniadakis, Learning nonlinear operators via deeponet based on the universal approximation theorem of operators, *Nature machine intelligence* (2021).
- [16] D. Pereira, F. Afonso, F. Lau, End-to-end deep-learning-based surrogate modeling for supersonic airfoil shape optimization, *Aerospace* 12 (2025). doi:10.3390/aerospace12050389.
- [17] Y. Y. Liu, J. X. Shen, P. P. Yang, X. W. Yang, A cnn-pinn-drl driven method for shape optimization of airfoils, *Engineering Applications of Computational Fluid Mechanics* (2025).
- [18] D. Rajnarayan, A. Ning, J. A. Mehr, Universal airfoil parametrization using b-splines, in: 2018 Applied Aerodynamics Conference, 2018, p. 3949.
- [19] P. Della Vecchia, E. Daniele, E. D'Amato, An airfoil shape optimization technique coupling parsec parameterization and evolutionary algorithm, *Aerospace Science and Technology* (2014).
- [20] W. He, X. Liu, Improved aerofoil parameterisation based on class/shape function transformation, *The Aeronautical Journal* (2019).
- [21] B. Kulfan, A Universal Parametric Geometry Representation Method - "CST", *Aerospace Sciences Meetings, American Institute of Aeronautics and Astronautics*, 2007. doi:10.2514/6.2007-62, 0.
- [22] N. Vu, J. Lee, Aerodynamic design optimization of helicopter rotor blades including airfoil shape for forward flight, *Aerospace Science and Technology* 42 (2015) 106–117.
- [23] Y. Zhang, X. Fang, H. Chen, S. Fu, Z. Duan, Y. Zhang, Supercritical natural laminar flow airfoil optimization for regional aircraft wing design, *Aerospace Science and Technology* (2015).
- [24] D. J. Toal, N. W. Bressloff, A. J. Keane, C. M. Holden, Geometric filtration using proper orthogonal decomposition for aerodynamic design optimization, *AIAA journal* (2010).
- [25] X. Wu, W. Zhang, X. Peng, Z. Wang, Benchmark aerodynamic shape optimization with the pod-based cst airfoil parametric method, *Aerospace Science and Technology* (2019).
- [26] J. Li, M. A. Bouhlef, J. R. Martins, Data-based approach for fast airfoil analysis and optimization, *AIAA Journal* (2019).
- [27] K. Yonekura, K. Suzuki, Data-driven design exploration method using conditional variational autoencoder for airfoil design, *Structural and Multidisciplinary Optimization* (2021).
- [28] G. Achour, W. J. Sung, O. J. Pinon-Fischer, D. N. Mavris, Development of a Conditional Generative Adversarial Network for Airfoil Shape Optimization, *AIAA SciTech Forum, American Institute of Aeronautics and Astronautics*, 2020. doi:10.2514/6.2020-2261, 0.
- [29] W. Chen, K. Chiu, M. D. Fuge, Airfoil design parameterization and optimization using bézier generative adversarial networks, *AIAA journal* (2020).
- [30] V. Sekar, Q. Jiang, C. Shu, B. C. Khoo, Fast flow field prediction over airfoils using deep learning approach, *Physics of Fluids* (2019).
- [31] M. Giselle Fernández-Godino, Review of multi-fidelity models, *Advances in Computational Science and Engineering* 1 (2023) 351–400. doi:10.3934/acse.2023015.
- [32] M. Schouler, A. Belme, P. Cinnella, Comparison of multi-fidelity surrogate models for multi-objective aerodynamic optimization in turbomachinery under extreme cost imbalance, *Advanced Modeling and Simulation in Engineering Sciences* 12 (2025) 35. doi:10.1186/s40323-025-00316-3.
- [33] N. M. Alexandrov, R. M. Lewis, C. R. Gumbert, L. L. Green, P. A. Newman, Approximation and model management in aerodynamic optimization with variable-fidelity models, *Journal of Aircraft* 38 (2001) 1093–1101. doi:10.2514/2.2877.
- [34] V. O. Balabanov, A. A. Giunta, O. Golovidov, B. Grossman, W. H. Mason, L. T. Watson, R. T. Haftka, Reasonable design space approach to response surface approximation, *Journal of Aircraft* 36 (1999) 308–315. doi:10.2514/2.2438.
- [35] J. Zheng, X. Shao, L. Gao, P. Jiang, Z. Li, A hybrid variable-fidelity global approximation modelling method combining tuned radial basis function base and kriging correction, *Journal of Engineering Design* 24 (2013). doi:10.1080/09544828.2013.788135.
- [36] C. C. Fischer, R. V. Grandhi, P. S. Beran, Bayesian low-fidelity correction approach to multi-fidelity aerospace design, in: 58th AIAA/ASCE/AHS/ASC Structures, Structural Dynamics, and Materials Conference, 2017, p. 0133.
- [37] M. Schouler, A. Belme, P. Cinnella, Bayesian and non-bayesian multi-fidelity surrogate models for multi-objective aerodynamic optimization under extreme cost imbalance, 2025. URL: <https://arxiv.org/abs/2505.17279>. arXiv:2505.17279.
- [38] P. Z. G. Qian, C. F. J. Wu, Bayesian hierarchical modeling for integrating low-accuracy and high-accuracy experiments, *Technometrics* 50 (2008) 192–204. doi:10.1198/004017008000000082.
- [39] A. I. Forrester, A. J. Keane, Recent advances in surrogate-based optimization, *Progress in Aerospace Sciences* 45 (2009) 50–79. doi:<https://doi.org/10.1016/j.paerosci.2008.11.001>.
- [40] L. L. Gratiet, J. Garnier, Recursive co-kriging model for design of computer experiments with multiple levels of fidelity, *International Journal for Uncertainty Quantification* 4 (2014) 365–386. doi:10.1615/Int.J.UncertaintyQuantification.2014006914.

- [41] L. Brevault, M. Balesdent, A. Hebbal, Overview of gaussian process based multi-fidelity techniques with variable relationship between fidelities, application to aerospace systems, *Aerospace Science and Technology* 107 (2020) 106339. doi:<https://doi.org/10.1016/j.ast.2020.106339>.
- [42] X. Meng, G. E. Karniadakis, A composite neural network that learns from multi-fidelity data: Application to function approximation and inverse pde problems, *Journal of Computational Physics* 401 (2020) 109020. doi:<https://doi.org/10.1016/j.jcp.2019.109020>.
- [43] X. Meng, H. Babae, G. E. Karniadakis, Multi-fidelity bayesian neural networks: Algorithms and applications, *Journal of Computational Physics* 438 (2021) 110361. URL: <https://www.sciencedirect.com/science/article/pii/S0021999121002564>. doi:<https://doi.org/10.1016/j.jcp.2021.110361>.
- [44] K. Cutajar, M. Pullin, A. Damianou, N. Lawrence, J. González, Deep gaussian processes for multi-fidelity modeling, 2019. URL: <https://arxiv.org/abs/1903.07320>. arXiv:1903.07320.
- [45] A. A. Howard, M. Perego, G. E. Karniadakis, P. Stinis, Multifidelity deep operator networks for data-driven and physics-informed problems, *Journal of Computational Physics* 493 (2023) 112462. doi:<https://doi.org/10.1016/j.jcp.2023.112462>.
- [46] S. Bhola, S. Pawar, P. Balaprakash, R. Maulik, Multi-fidelity reinforcement learning framework for shape optimization, *Journal of Computational Physics* 482 (2023) 112018. doi:<https://doi.org/10.1016/j.jcp.2023.112018>.
- [47] K. Li, F. Li, Multi-fidelity methods for optimization: A survey, 2024. URL: <https://arxiv.org/abs/2402.09638>. arXiv:2402.09638.
- [48] X. Zhang, F. Xie, T. Ji, Z. Zhu, Y. Zheng, Multi-fidelity deep neural network surrogate model for aerodynamic shape optimization, *Computer Methods in Applied Mechanics and Engineering* 373 (2021) 113485. doi:<https://doi.org/10.1016/j.cma.2020.113485>.
- [49] P. MOHAMMAD ZADEH, M. SAYADI, An efficient aerodynamic shape optimization of blended wing body uav using multi-fidelity models, *Chinese Journal of Aeronautics* 31 (2018) 1165–1180. doi:<https://doi.org/10.1016/j.cja.2018.04.004>.
- [50] C. M. Aye, K. Wansaseub, S. Kumar, G. G. Tejani, S. Bureerat, A. R. Yildiz, N. Pholdee, Airfoil shape optimisation using a multi-fidelity surrogate-assisted metaheuristic with a new multi-objective infill sampling technique, *CMES - Computer Modeling in Engineering and Sciences* 137 (2023) 2111–2128. doi:<https://doi.org/10.32604/cmescs.2023.028632>.
- [51] X. Zhang, F. Xie, T. Ji, Z. Zhu, Y. Zheng, Multi-fidelity deep neural network surrogate model for aerodynamic shape optimization, *Computer Methods in Applied Mechanics and Engineering* 373 (2021) 113485. doi:<https://doi.org/10.1016/j.cma.2020.113485>.
- [52] R. Charayron, T. Lefebvre, N. Bartoli, J. Morlier, Towards a multi-fidelity & multi-objective bayesian optimization efficient algorithm, *Aerospace Science and Technology* 142 (2023) 108673. doi:<https://doi.org/10.1016/j.ast.2023.108673>.
- [53] X. Wu, Z. Zuo, L. Ma, W. Zhang, Multi-fidelity neural network-based aerodynamic optimization framework for propeller design in electric aircraft, *Aerospace Science and Technology* 146 (2024) 108963. doi:<https://doi.org/10.1016/j.ast.2024.108963>.
- [54] N. Mourousias, B. G. Marinus, M. C. Runacres, A novel multi-fidelity optimization framework for high-altitude propellers, *Aerospace Science and Technology* 153 (2024) 109407. doi:<https://doi.org/10.1016/j.ast.2024.109407>.
- [55] I. Robledo, Y. Li, G. Y. Cornejo Maceda, R. Castellanos, Fast and robust parametric and functional learning with hybrid genetic optimisation (hygo), *Advances in Engineering Software* 216 (2026) 104139. doi:[10.1016/j.advengsoft.2026.104139](https://doi.org/10.1016/j.advengsoft.2026.104139).
- [56] M. Drela, Xfoil: An analysis and design system for low reynolds number airfoils, in: T. J. Mueller (Ed.), *Low Reynolds Number Aerodynamics*, Springer Berlin Heidelberg, Berlin, Heidelberg, 1989, pp. 1–12.
- [57] J. Morgado, R. Vizinho, M. Silvestre, J. Páscoa, Xfoil vs cfd performance predictions for high lift low reynolds number airfoils, *Aerospace Science and Technology* (2016). doi:<https://doi.org/10.1016/j.ast.2016.02.031>.
- [58] S. Zhang, H. Li, A. A. Abbasi, Design methodology using characteristic parameters control for low reynolds number airfoils, *Aerospace Science and Technology* (2019). doi:<https://doi.org/10.1016/j.ast.2019.01.003>.
- [59] M. Carreño Ruiz, D. D'Ambrosio, Experimental validation of virtual wind tunnel testing for ultra-low reynolds numbers flows, *Aerotecnica Missili & Spazio* (2024).
- [60] H. Jasak, Openfoam: Open source cfd in research and industry, *International Journal of Naval Architecture and Ocean Engineering* 1 (2009) 89–94. URL: <https://www.sciencedirect.com/science/article/pii/S2092678216303879>. doi:<https://doi.org/10.2478/IJNAOE-2013-0011>.
- [61] F. R. Menter, Two-equation eddy-viscosity turbulence models for engineering applications, *AIAA journal* (1994).

- [62] D. C. Jespersen, T. H. Pulliam, M. L. Childs, Overflow turbulence modeling resource validation results, Technical Report ARC-E-DAA-TN35216, NASA Ames Research Center, 2016. URL: <https://ntrs.nasa.gov/citations/20190000252>.
- [63] F. R. Menter, Improved Two-Equation k-omega Turbulence Models for Aerodynamic Flows, Technical Report NASA-TM-103975, NASA Ames Research Center, 1992. URL: <https://ntrs.nasa.gov/citations/19930013620>, NASA Technical Memorandum.
- [64] J. A. Nelder, R. Mead, A simplex method for function minimization, *The Computer Journal* 7 (1965) 308–313.
- [65] C. A. Coello Coello, Theoretical and numerical constraint-handling techniques used with evolutionary algorithms: a survey of the state of the art, *Computer Methods in Applied Mechanics and Engineering* 191 (2002) 1245–1287. doi:[https://doi.org/10.1016/S0045-7825\(01\)00323-1](https://doi.org/10.1016/S0045-7825(01)00323-1).